Flow fields around the Emperor Seamounts detected from current data

Taku Wagawa,[1] Yutaka Yoshikawa,[2] Yutaka Isoda,[3] Eitarou Oka,[4,5] Kazuyuki Uehara,[6] Toshiya Nakano,[7] Kenshi Kuma,[3] and Shogo Takagi[8]

Received 19 August 2011; revised 25 March 2012; accepted 19 April 2012; published 7 June 2012.

[1] Bathymetric influences of the Emperor Seamounts (ESs) on the local and large-scale flow fields in the subarctic North Pacific were investigated by analyzing data of directly measured velocity obtained using Argo floats, near-surface buoys, and moored current meters. The local influences were evident in notable deflections of two relatively strong ($\sim$0.05 m s^{-1}) eastward flows over ESs. A Taylor cap induced by the eastward flow impinging against the Nintoku Seamount (around 42.0°N, 170.5°E) was clearly identified in the climatological flow field at 1000 m depth. This flow pattern was also identified in the near-surface flow field (15 m depth) and dynamic height field at 200 dbar relative to 2000 dbar, indicating the Taylor cap is stable or frequently generated and extends to the surface. An anticyclonic flow was found over the Suiko Seamount (around 45.0°N, 170.5°E). The influences on the large-scale flow field were found in data obtained from current meters moored over the southeastern flank of the Suiko Seamount and Argo float trajectories. These data indicate for the first time from velocity observations that there is a seasonally varying boundary current along the eastern side of ESs partially compensating for the Sverdrup transport to the east of ESs, and hence, the seasonally varying component of the subarctic gyre in the North Pacific is divided into two subgyres by ESs.

Citation: Wagawa, T., Y. Yoshikawa, Y. Isoda, E. Oka, K. Uehara, T. Nakano, K. Kuma, and S. Takagi (2012), Flow fields around the Emperor Seamounts detected from current data, *J. Geophys. Res.*, *117*, C06006, doi:10.1029/2011JC007530.

1. Introduction

[2] The subarctic North Pacific has been the subject of recent climate studies because of its major role in the long-term variability of the Earth's climate [e.g., *Mann and Park*, 1996; *White and Cayan*, 1998]. This region has also been studied extensively from a fisheries viewpoint because it is known for high biological productivity supported by nutrient-rich water [e.g., *Saijo and Ichimura*, 1960; *Taniguchi and Kawamura*, 1972; *Takahashi and Ichimura*, 1972; *Kasai et al.*, 1997; *Taniguchi*, 1999]. To clearly understand the mechanisms of climate variation or the habitat selectivity of fisheries resources, we need detailed understanding of the flow fields in the subarctic North Pacific, which controls horizontal distributions of temperature and salinity (T–S) and various other material properties.

[3] The flow field of the subarctic North Pacific is thought to be strongly affected by bathymetry since density stratification and hence the baroclinic component of the circulation in that region is relatively weak over timescales of a year [e.g., *Levine and White*, 1981; *Roden*, 1984; *Kono and Kawasaki*, 1997; *Ito et al.*, 2004; *Kuragano and Kamachi*, 2004; *Wagawa et al.*, 2006, 2010]. The Emperor Seamounts (ESs) are notable bathymetric features in the subarctic North Pacific [*Dietz*, 1954]. They range approximately from 35°N to 52°N along about 170°E and cross almost the whole region of the subarctic North Pacific, as shown in Figure 1. ESs are very high and steep; the top of the highest seamount is at about 1300 m depth. Therefore, large bathymetric influences of ESs on the flow field of the subarctic North Pacific are expected.

[4] Bathymetric influences of ESs on a local flow field and hydrographic structure have been debated by several studies [*Levine and White*, 1981, 1983; *Roden*, 1984, 1987]. Using accumulated expendable bathythermograph data, *Levine and White* [1983] showed that surface fronts are sometimes deflected around the Shatsky Rise and Hess Rise

[1]Tohoku National Fisheries Research Institute, Shiogama, Japan.
[2]Research Institute for Applied Mechanics, Kyushu University, Kasuga, Japan.
[3]Graduate School of Fisheries Science, Hokkaido University, Hakodate, Japan.
[4]Atmosphere and Ocean Research Institute, University of Tokyo, Kashiwa, Japan.
[5]Research Institute for Global Change, Japan Agency for Marine-Earth Science and Technology, Yokosuka, Japan.
[6]School of Marine Science and Technology, Tokai University, Shizuoka, Japan.
[7]Global Environment and Marine Department, Japan Meteorological Agency, Tokyo, Japan.
[8]School of Fisheries Science, Hokkaido University, Hakodate, Japan.

Corresponding author: T. Wagawa, Tohoku National Fisheries Research Institute, Shinhama-cho, Shiogama, Miyagi 985-0001, Japan. (wagawa@affrc.go.jp)

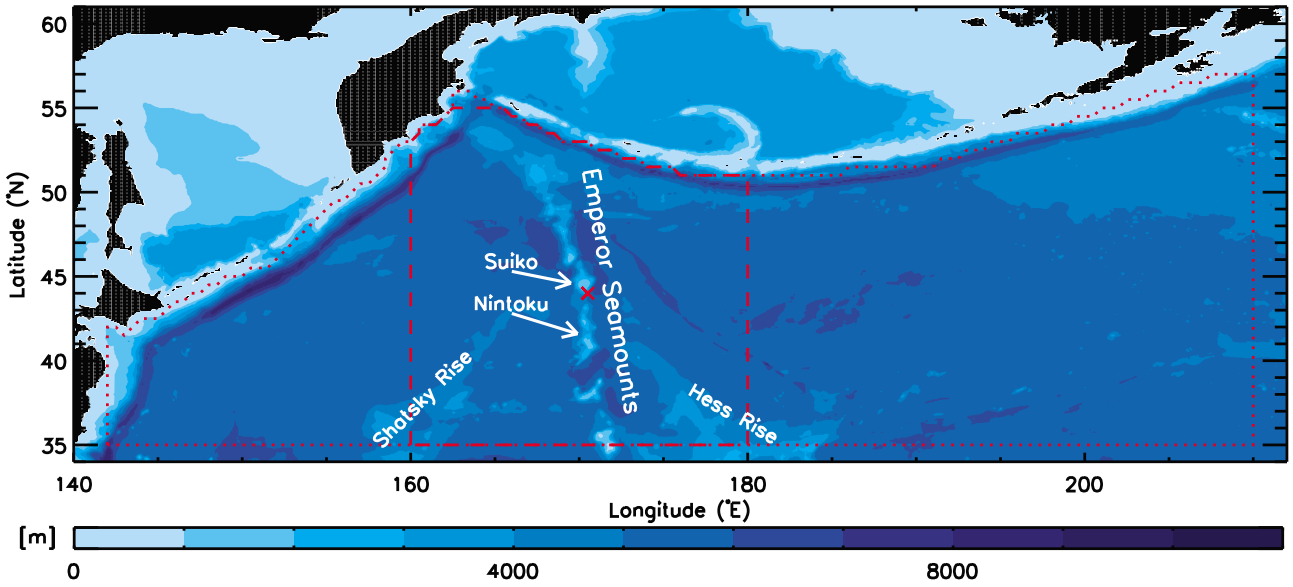

Figure 1. Bottom topography around the Emperor Seamounts (ESs) in the subarctic North Pacific. The red dashed line represents the area investigated for the local effects of the ESs (section 3), while the red dotted line shows the area examined for large-scale effects of the ESs (section 4). The red cross indicates the observation point for moored current meters.

(located near ESs; Figure 1) and bifurcated around ESs. *Roden* [1984, 1987] analyzed three years of hydrographic data and showed that surface fronts and corresponding baroclinic flows are deflected around ESs. They suggested that intense frontal meanders or eddies are associated with steep bathymetries. *Wagawa et al.* [2006] analyzed six years of hydrographic data and found that two surface fronts and corresponding baroclinic flows approaching ESs merge when passing over the narrow gap between the seamounts. Note that these studies analyzed hydrographic data and discussed only the *relative* geostrophic current (i.e., baroclinic components), although large barotropic components are expected in this region. To better understand the flow field affected by seamount topography, directly observed velocity data including the barotropic components should be analyzed.

[5] ESs are expected to affect not only a local flow field as mentioned above but also the large-scale subarctic gyre of the North Pacific. This gyre is a cyclonic circulation driven by positive wind stress curl [e.g., *Sekine*, 1999], and the effect of ESs on the gyre was first noted by *Kono and Kawasaki* [1997]. From moored current meters, they estimated the Oyashio (the western boundary current of the subarctic gyre) volume transport and compared it with the Sverdrup transport. They found that the Oyashio transport corresponds well with the Sverdrup transport integrated from ESs to the western boundary (the Japanese coast) rather than from the eastern boundary of the subarctic gyre (the west coast of North America). In addition, *Ito et al.* [2004] analyzed moored current meter data and satellite altimetry data; they showed that the Oyashio transport is better correlated with the Sverdrup transport integrated from ESs to the western boundary for shorter period such as the seasonal cycle. These findings imply that ESs act as a vertical wall dividing the subarctic gyre into two subgyres, and that a boundary current like the Oyashio flows along the eastern side of ESs. In fact, *Kuragano and Kamachi* [2004] represented such a boundary current along the eastern side of ESs in numerical experiments in which satellite and in situ T–S data were assimilated. *Wagawa et al.* [2010] examined the dependence of the boundary current on the seamount height and width and the density stratification in a series of simplified numerical experiments and suggested the high possibility of the presence of the boundary current along the actual ESs. These studies have suggested bathymetric influences of ESs on the large-scale subarctic gyre of the North Pacific. However, some studies [*Isoguchi et al.*, 1997; *Isoguchi and Kawamura*, 2006] considered that these bathymetric influences are negligible; they described that the width of ESs is so small that their effects are unimportant for the subarctic gyre. To confirm the bathymetric influences of ESs, the presence of the boundary current along ESs should be validated with in situ current measurements.

[6] One factor that has limited our understanding of the bathymetric influences of ESs is a paucity of direct measurements of velocity at middle and deep layers. Recently, trajectory data obtained using Argo floats, which can be used to estimate a mid-level or deep velocity field, have been accumulated. We also moored current meters to measure mid-level and deep velocities. This study aims to clarify the bathymetric influences of ESs on the flow field of the subarctic North Pacific using these directly measured velocity data. The data and methods used in the following are described in section 2. Results and a discussion are presented in sections 3–4. A summary is given in section 5.

2. Data Source and Field Observations

2.1. Argo Float Trajectories

[7] We used Argo float position data in the region enclosed by red dashed lines in Figure 1 (35.0°N–55.0°N and 160.0°E–180.0°E) from February 2000 through

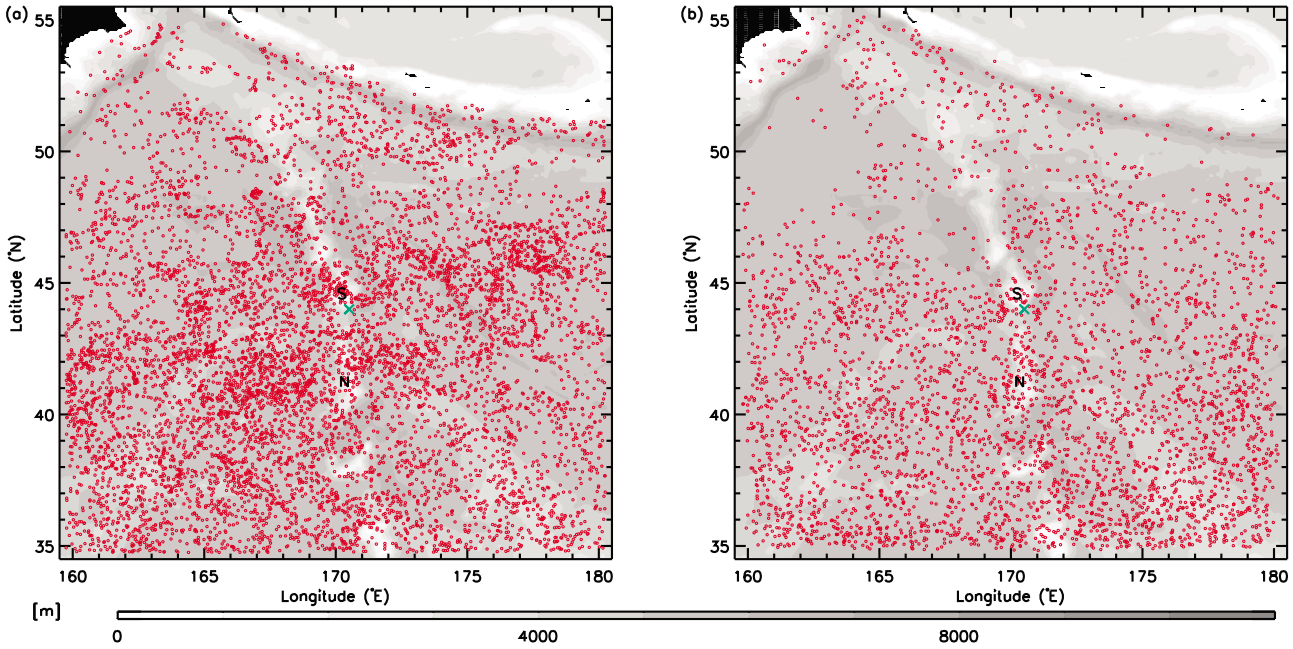

Figure 2. Data locations (red open circles) of (a) parking-depth velocities obtained from Argo floats and (b) drift velocities obtained from near surface buoys. The green cross indicates the location of moored current meters. Symbols "S" and "N" denote the Suiko and Nintoku Seamounts, respectively.

February 2010. A total of 7653 float position data were obtained by 175 Argo floats with parking depths greater than 1000 m. The data were downloaded from the Web site of the Argo Global Data Assembly Center.

[8] Velocities at the parking depth were evaluated from the float ARGOS position fixes applying extrapolation [e.g., *Park et al.*, 2005; *Menna and Poulain*, 2010]; the float diving and resurfacing locations were first estimated by extrapolating the ARGOS position fixes using the diving and resurfacing times which are derived from the float's metadata and fitting a linear drift and an inertial oscillation to the position fixes. Unfortunately, the diving and resurfacing times were often inaccurate or not reported by the float. In such cases, the times were inferred from the times of first and last ARGOS position fixes for a given surface trajectory and programmed residence time at the surface [*Willis and Fu*, 2008]. The parking-depth velocities were then obtained by dividing the distance between the diving and resurfacing locations by the elapsed time. The velocity data larger than 0.7 m s^{-1} were regarded as error and removed manually [*Book et al.*, 2002]. In our analysis, the position and time of the parking-depth velocities were defined as the middle of the diving and resurfacing positions and times. The location of data are indicated in Figure 2a.

[9] The velocity field on a regular grid (0.5° × 0.5°) was estimated using a method of the optimal interpolation in space for two-dimensional nondivergent vector field [*Papoulis*, 1972; *Bretherton et al.*, 1976]. Spatial means of the horizontal velocities were first calculated by taking arithmetic averages of the parking-depth velocities over the whole region and the mean velocities were subtracted from the parking-depth velocities. The optimal interpolation was then applied to the resulting anomaly fields and the mean velocities were finally added back into the interpolated anomaly fields. Space covariance functions used in the interpolation were

$$f(r) = -\frac{1}{r}\frac{\partial C(r)}{\partial r} = U^2\left(1+\frac{r}{R_c}\right)\exp\left(-\frac{r}{R_c}\right), \quad (1)$$

$$g(r) = -\frac{\partial^2 C(r)}{\partial r^2} = U^2\left(1+\frac{r}{R_c}-\frac{r^2}{R_c^2}\right)\exp\left(-\frac{r}{R_c}\right), \quad (2)$$

$$C(r) = \Phi^2\left(1+\frac{r}{R_c}+\frac{1}{3}\frac{r^2}{R_c^2}\right)\exp\left(-\frac{r}{R_c}\right), \quad (3)$$

where $f(r)$ and $g(r)$ are the longitudinal and transverse covariance functions as a function of distance ($r = \sqrt{x^2+y^2}$), respectively, $C(r)$ is the covariance function of the corresponding stream function field and U^2 and Φ^2 ($=3U^2R_c^2$) are the variances of velocities and stream functions, respectively. The characteristic length scale (R_c) was set to 100 km. In the above, the data within 150 km from a cell center (L_0 = 150 km) were used. Variances of velocities, stream functions and measurement errors were calculated by extrapolating the observed structure function [*Mizuno*, 1995]. The cells where the ratios of the velocity estimation errors (that are also obtained from the optimal estimation) to the estimated velocities larger than 0.1 were regarded as missing. These parameters and threshold values were used unless otherwise noted. We adopted grid spacing (0.5° ≈ 40 km) smaller than the width of ESs (100 ∼ 200 km) and the short characteristic length scale to investigate the effects of the seamounts on a detailed velocity field.

[10] Since the number of floats was not high enough to illustrate the flow field at each parking depth (111 floats at 1000 m depth, 30 floats at 1500 m depth, 2 floats at 1650 m depth and 32 floats at 2000 m depth), we calculated the velocities at a depth of 1000 m from the velocities at the other depths with climatological geostrophic shears [e.g., *Lavender et al.*, 2005; *Willis and Fu*, 2008]. The geostrophic shears were computed from T–S data of the World Ocean Atlas 2001 climatology [*Boyer et al.*, 2005].

[11] There are two sources of error in the estimates of the parking-depth velocity. One is associated with estimating either diving or resurfacing locations by extrapolating ARGOS position fixes. To assess this uncertainty, we artificially predicted the last (n-th; n is the number of ARGOS position fixes in the surface cycle) point fix by extrapolating the previous ($<n$-th) point fixes and compared it with the actual last fix (which is known) in the same way as described by *Park et al.* [2005], *Chen et al.* [2007] and *Menna and Poulain* [2010]. In the present data set with $n \geq 6$, the distances between the predicted and the actual position fixes had a median of about 740 m.

[12] The second error source is related to the velocity shear above the parking depth. The velocity shear is assumed to follow the shape of the first baroclinic mode and is constructed from the difference in climatological geostrophic velocities between the surface and 2000 m depth [e.g., *Park et al.*, 2005; *Willis and Fu*, 2008; *Menna and Poulain*, 2010] estimated using the T–S data of the World Ocean Atlas 2001 climatology [*Boyer et al.*, 2005]. The ascent time (the time taken for ascent from the parking depth to the surface) was not reported for about 31% of floats. In such cases, a median ascent time of the remaining 69% floats was used as an approximation [e.g., *Willis and Fu*, 2008]. In the present data set, the climatological velocity difference was 0.011 m s^{-1} and the median ascent time was 4.6 hours. Assuming an ascent rate is constant, the computed extra float drifts during ascent had a median of about 184 m. As argued by *Park et al.* [2005] and *Chen et al.* [2007], we approximated the descending float drift with the same distance (184 m).

[13] Since the estimation errors are uncorrelated, the total uncertainty can be evaluated as $\sqrt{2 \times (740\,\mathrm{m})^2 + 2 \times (184\,\mathrm{m})^2} \simeq 1078$ m. Dividing by 182.0 hours, the average residence time of the floats below the surface, the total drift uncertainty led to an error estimate of about 0.002 m s^{-1} for the parking-depth velocities. This error is small enough to allow detailed analysis of the relationship between the mid/deep-layer flow patterns and bathymetry.

2.2. Argo Float CTD Profiles

[14] We also used 4215 T–S profiles obtained by 145 Argo floats from June 2001 to March 2010 in the same region and period as those of the trajectory data (the region enclosed by red dashed lines in Figure 1). Only profiles with a maximum profiling depth greater than 2000 dbar were used in the present analysis to investigate the mid/deep hydrographic feature. In addition, we used only the profiles evaluated as "good" in the delayed quality controlled data of the Argo Global Data Assembly Center to avoid pressure bias errors. The T–S profiles were vertically averaged in 100 layers from 20 dbar to 2000 dbar at 20 dbar intervals. They were then horizontally interpolated for each cell as was done for the parking-depth velocities (section 2.1) except using the space covariance function for dynamic height field whose functional form is given by equation (3).

2.3. Surface Drift Buoys

[15] To examine the bathymetric influences on the near-surface flows, drift velocities of near-surface buoys (at 15 m depth) were used. We used 152,240 drift velocity (304,480 float position) data obtained by 286 buoys in the same region as that of the Argo float data (the region enclosed by red dashed lines in Figure 1) from November 1990 to September 2009. The data were downloaded from the Web site of the Atlantic Oceanographic and Meteorological Laboratory of the National Oceanic and Atmospheric Administration (NOAA/AOML). Preliminary quality control of the velocity data was carried out by NOAA/AOML. Near-surface drift velocities of each buoy are calculated from the buoy positions transmitted to satellites every 1.2–1.5 hours, and they are interpolated via kriging to regular six-hour intervals [*Hansen and Poulain*, 1996]. We computed the wind-driven (Ekman) velocity at 6-hourly intervals along the drifter track using the empirical formula of *Niiler et al.* [2003]

$$\mathrm{u_E} = \alpha f^{-1/2} \mathrm{W} \exp(i\beta), \tag{4}$$

where $\mathrm{u_E} = u_E + iv_E$ is the Ekman current at 15 m depth, $\alpha = 7 \times 10^{-7}$ $\mathrm{s}^{-1/2}$ relates to the speed factor of the wind-driven flow with respect to the wind speed, i is the imaginary unit, f is the Coriolis parameter and $\mathrm{W} = W_x + iW_y$ is 10 m height wind of the National Centers for Environmental Prediction (NCEP) reanalysis interpolated to each drifter track and $\beta = -54°$ represents the deflection angle of the wind-driven flow relative to the wind. The Ekman velocity ($\mathrm{u_E}$) was subtracted from the drift velocities. These velocity data were then averaged every 10 day (over 40 samples) in order for its timescale to be matched with that of the parking-depth velocities of Argo floats. The velocity data were then gridded using the same optimal interpolation as used for the parking-depth velocities (section 2.1). The location of data are indicated in Figure 2b.

2.4. Moored Current Meters

[16] To investigate the vertical structure and the temporal variation of flows near ESs, the velocities obtained from moored current meters were investigated. The observations of the current velocity with moored current meters (RCM8; Aanderaa Data Instruments) were conducted for about one year from July 26 in 2006 to July 7 in 2007 on the southeastern slope of the Suiko Seamount (44.0°N, 170.5°E and water depth of 3552 m; red cross in Figure 1). The mooring was deployed on the 169-th cruise of the T/S Oshoro-Maru (Hokkaido University) and recovered on the 180-th cruise. At the mooring, three current meters at about 1000 m, 2000 m and 3000 m depths were set and hourly velocity data were obtained. Tidal harmonic analysis was then performed to remove 49 tidal components: 48 tidal components that can be decomposed from the M_2 tidal component in our

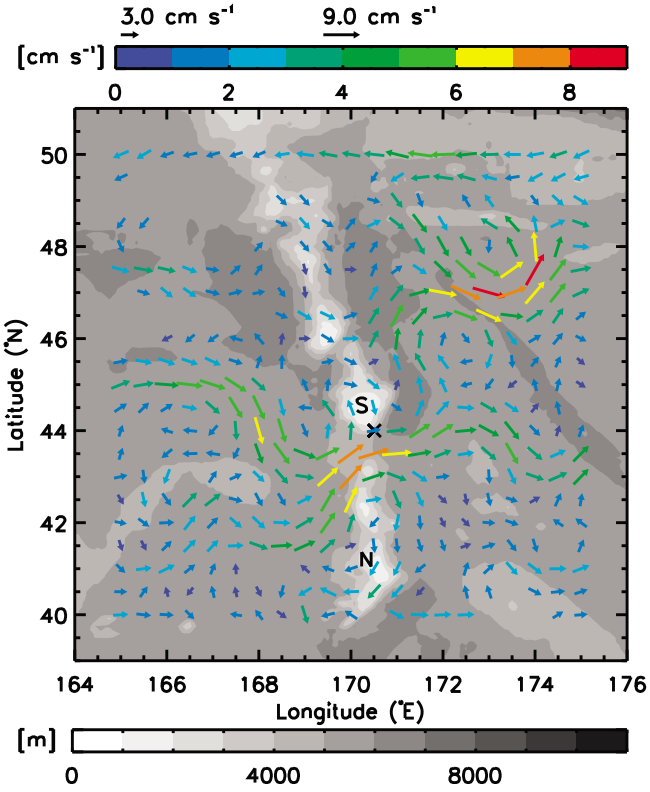

Figure 3. Climatological velocity vector at 1000 m depth estimated from Argo float trajectories. In the cells where the ratios of the velocity estimation errors to the estimated velocities are larger than 0.1, the vectors are not depicted regarding as missing. Both color and length of the arrow represent the velocity magnitude. Black cross indicates the position of the moored current meters. Symbols "S" and "N" denote the Suiko and Nintoku Seamounts, respectively.

observational period of 345 days (from M_2 to θ_1) and the M_f tidal component (which had high energy).

3. Bathymetric Influences of Emperor Seamounts on the Local Flow Field

[17] Figure 3 shows the horizontal distributions of the climatological velocity vector at 1000 m depth estimated from the Argo float trajectories. There were two relatively strong (~0.05 m s^{-1}) eastward flows at 42°N and 45°N to the west of the ESs (170°E), and these flows were deflected over the ESs and other major bathymetric features. This result clearly indicates the bathymetric influences of ESs on the flow field in the mid/deep layer, which were not obvious in previous large-scale circulation studies such as *Reid* [1997]. Similar features are found in summer hydrographic data sets of *Roden* [1984, 1987]. The present analysis (of the data including all seasons) clarifies that these features are deep and stable or frequently generated over timescales of a year.

[18] A more detailed examination of Figure 3 reveals an anticyclonic flow pattern over the Nintoku Seamount. A similar flow pattern was found in the climatological surface flow field derived from surface drift buoys (Figure 4), in which the anticyclonic flow pattern was embedded in a northern part of the S-shaped meandering of the eastward flow-passing over the Nintoku Seamount. The S-shaped flow pattern can also be identified in the climatological dynamic height field at 200 dbar relative to 2000 dbar estimated from Argo float T–S profiles (Figure 5). These results show that the bathymetric influences of the Nintoku Seamount extend to the surface.

[19] A similar flow pattern is found in the summer hydrographic data of *Roden* [1984] (see his Figure 14) and *Roden and Taft* [1985]. They suggested that the flow is a part of the Taylor cap formed by the impinging flow on the Nintoku Seamount. The S-shaped flow pattern found in the present results is similar to the theoretical pattern of the Taylor cap [e.g., *Verron and LeProvost*, 1985]. Note that the Taylor cap can be identified even in the climatological surface flow field; it is stable or frequently generated and extends to the surface. This result is consistent with results of *Chapman and Haidvogel* [1992], who performed a series of idealized numerical experiments for Taylor caps. For stratified flows over a tall seamount (Burger number $NH/fL \geq 1$ and $H_m/H \simeq 0.8$, which are typical around the Nintoku Seamount, where N, H, f, L and H_m are the Brunt-Väisälä frequency (≈0.002 s^{-1}), water depth (≈6000 m), the Coriolis parameter (≈10^{-4} s^{-1}), seamount width (≈10^5 m) and seamount height (≈5000 m)), steady Taylor caps can be generated if the Rossby number ($Ro = U/fL$, where U is the impinging flow velocity) is below the critical Rossby number (Ro_c = 0.15) [*Chapman and Haidvogel*, 1992]. Around the Nintoku Seamount, the characteristic flow velocity (U) was smaller than 0.3 m s^{-1} (Figures 3 and 4),

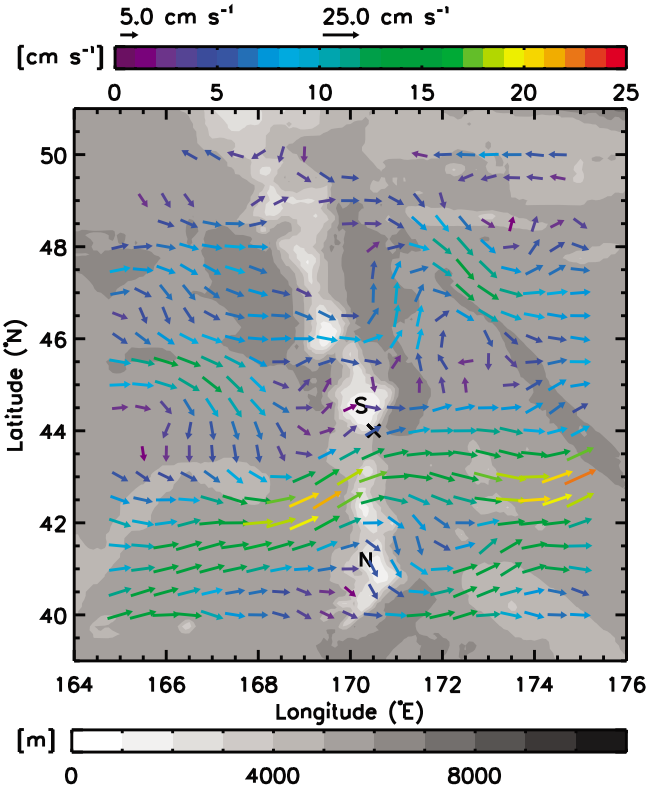

Figure 4. Same as Figure 3 except for data of the drift velocities obtained from near-surface (15 m depth) buoys.

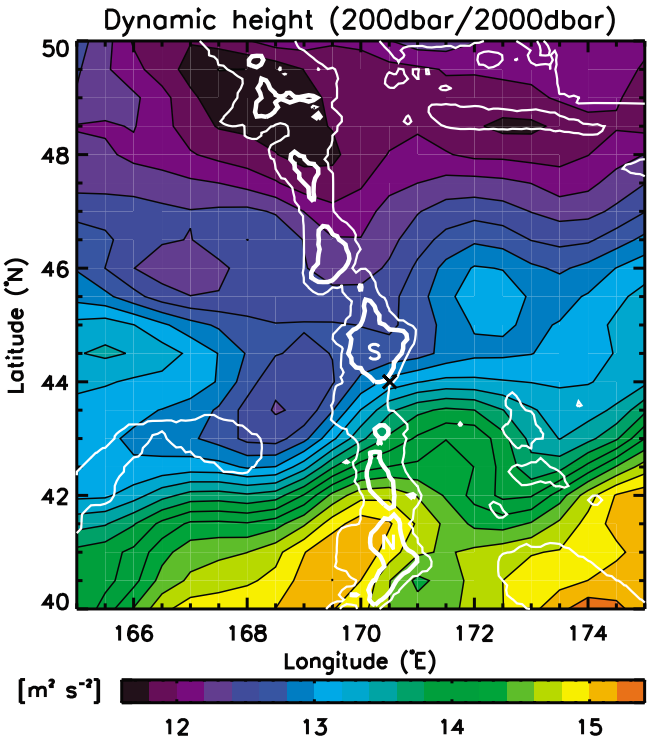

Figure 5. Climatological dynamic height at 200 dbar relative to 2000 dbar estimated from Argo float T–S profiles. White thick and thin contours indicate 3000 m depth and 5000 m depth, respectively. Black cross indicates the position of the moored current meters. Symbols "S" and "N" denote the Suiko and Nintoku Seamounts, respectively.

and hence, the Rossby number was well below the critical value ($Ro < 0.03 < Ro_c$).

[20] The other eastward flow at 45°N appeared to be steered southward near 167°E–168°E along the northeastern slope of the Shatsky Rise. The flow then flowed to the east over the gap between Suiko and Nintoku Seamounts and then flowed to the north over the eastern flank of the Suiko Seamount. The climatological surface velocity field (Figure 4) and dynamic height field (Figure 5) also show this flow pattern. Although the eastward flow at 45°N does not seem to impinge on the Suiko Seamount in the climatological flow fields, close examination of the flow field over the Suiko Seamount reveals anticyclonic flow over the Suiko Seamount. This was clear in the high-resolution horizontal distributions (0.25° × 0.25° grid) of the velocity vectors (Figure 6). The anticyclonic flow was also evident in the trajectory paths (Figure 7), which show trapping of several floats over the seamount.

[21] *Roden* [1984] and *Roden and Taft* [1985] found the flow patterns of Taylor caps over the Suiko Seamount and described the caps as being more predominant than the cap over the Nintoku Seamount. However, such features were not clearly found in the climatological flow fields; the flow patterns of Taylor caps was more predominant over the Nintoku Seamount than over the Suiko Seamount (Figures 3–5). One possible explanation for the discrepancy is that the flow does not always impinge against the Suiko Seamount and the Taylor cap is thus transient; therefore, the Taylor cap over the Suiko Seamount is less clear than that over the Nintoku Seamount in the climatological field (Figures 3–5). However, the anticyclonic flow was identified over the Suiko Seamount in the climatological flow field (Figures 3 and 4). The trajectory paths show that some of the floats trapped over the Suiko Seamount are not traced back to the eastward impinging flow (Figure 7). Different scenario is required for the generation of the anticyclonic eddy.

[22] Current variability over the Suiko Seamount can be investigated in detail using the velocity data obtained from moored current meters. The daily means of the processed hourly velocity data were calculated by taking the 25-hour running mean and subsampling at intervals of 1 day. Figure 8 shows the daily current velocities during our observation. Noticeable temporal variations are evident, and they were larger at greater depths; root-mean square velocity fluctuations were 0.014 m s^{-1} at 1000 m depth, 0.019 m s^{-1} at 2000 m depth and 0.021 m s^{-1} at 3000 m depth. Figure 9 represents the rotary spectrum of the current velocity. Significant peak in the spectrum was found at 10–12-day (240–288-hour) period at 3000 m depth, and power spectra were larger at greater depths; total rotary spectra at 10-day (240-hour) period were 6.1 × 10^{-7} (m s^{-1})^2 cph^{-1} at 1000 m depth, 6.1 × 10^{-6} (m s^{-1})^2 cph^{-1} at 2000 m depth and 1.6 × 10^{-5} (m s^{-1})^2 cph^{-1} at 3000 m depth. Sources of these bottom-intensified disturbances are unknown; they might be excited by barotropic flows induced by the meandering of the oceanic frontal jet or atmospheric disturbances and propagate as bottom-trapped waves. Energetic eddies shown in Figure 7 seem related to those variations. In fact, *Isoda and Fukai* [2004] reported that there were often eddy-like motions over the Suiko Seamount from analysis of satellite altimetry data.

[23] These data allow us to speculate that the anticyclonic eddy over the Suiko Seamount is generated by eddy-

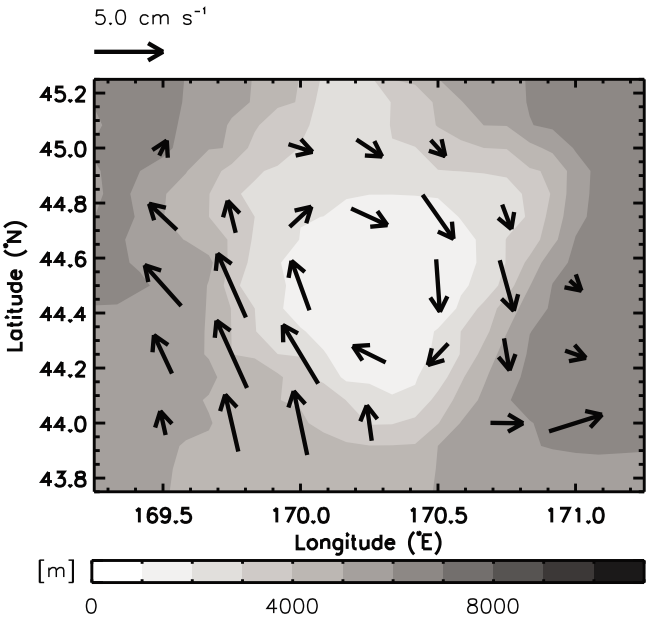

Figure 6. Same as Figure 3 except for a high-resolution grid (0.25° × 0.25°) cells with R_c = 50 km and L_0 = 75 km in order to show the anticyclonic circulation over the Suiko Seamount.

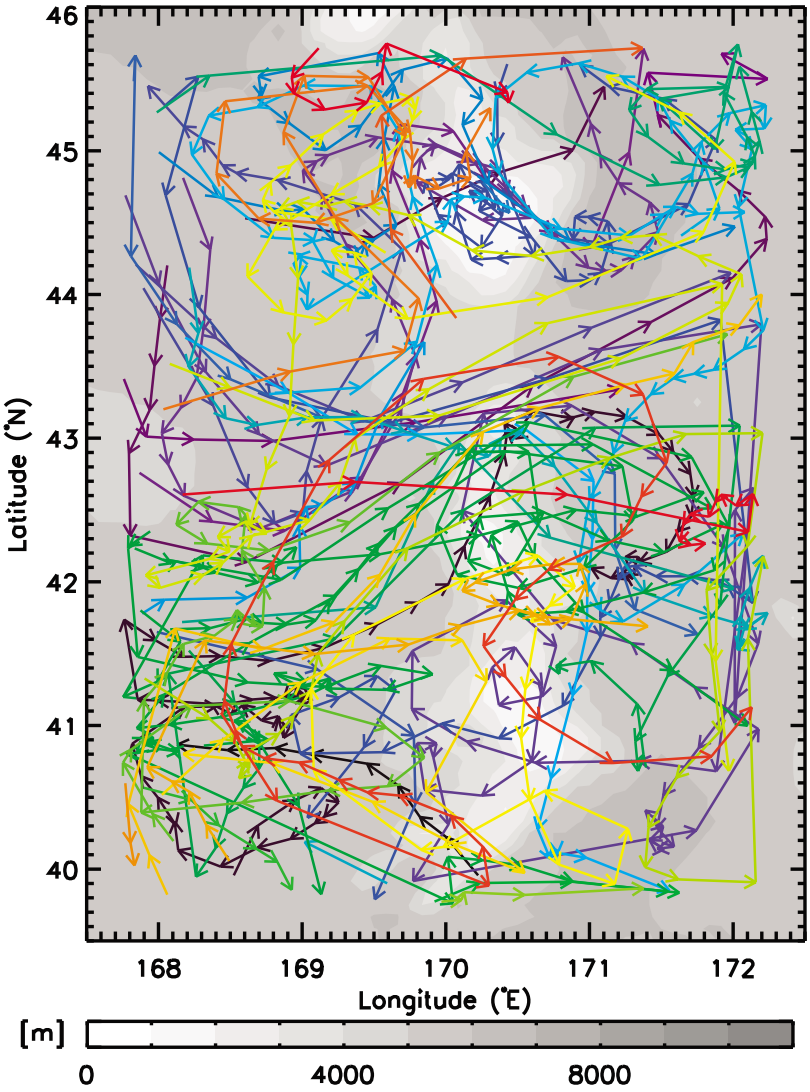

Figure 7. Trajectory paths of Argo floats around the Nintoku and Suiko Seamounts illustrated by connecting the locations of the parking-depth velocities.

topography interaction. It is well known that the mean current can be generated if these perturbations mix the potential vorticity of water across the slope [e.g., *Holloway*, 1987; *Adcock and Marshall*, 2000]. Such current is anticyclonic over a seamount. Thus, eddies may be cause of the formation of anticyclonic flow over the Suiko Seamount found in the climatological flow fields.

4. Bathymetric Influences of Emperor Seamounts on the Subarctic Gyre of the North Pacific

[24] *Kuragano and Kamachi* [2004] simulated the boundary current along the eastern side of ESs in their numerical assimilation. *Wagawa et al.* [2010] suggested the high possibility of the presence of the boundary current along the ESs. If the boundary current actually exists, it should covary with the interior Sverdrup flows to the east of ESs on shorter time-scales. This is because in the subarctic North Pacific where the density stratification is weak, the barotropic Rossby waves excited at the eastern boundary (the west coast of North America) propagate to ESs within a week whereas the baroclinic Rossby waves take more time (>10 years) to reach ESs and hence are damped to a larger degree before arriving at the ESs. The short baroclinic Rossby waves excited at the ESs due to incident long barotropic waves from the eastern boundary and the local wind forcing [e.g., *Wang and Koblinsky*, 1994] are expected to be damped quickly because of its large wave number and small group velocity [*Wagawa et al.*, 2010]. Thus, the phase of shorter fluctuations such as a seasonal variation in the boundary current is expected to be less affected by the baroclinic waves as found by *Qiu* [2002] and *Wagawa et al.* [2010]. This section focuses on the seasonal variations in the boundary current along ESs and the interior Sverdrup transport to the east.

[25] Figure 10 shows the horizontal distribution of the climatological monthly wind stress curl in winter (February) and summer (August) estimated from the daily wind stress data set of the NCEP reanalysis data set [*Kalnay et al.*, 1996]. Prominent seasonal variation in the wind stress curl field can be seen in the subarctic North Pacific; the wind stress curl was largest (smallest) in winter (summer).

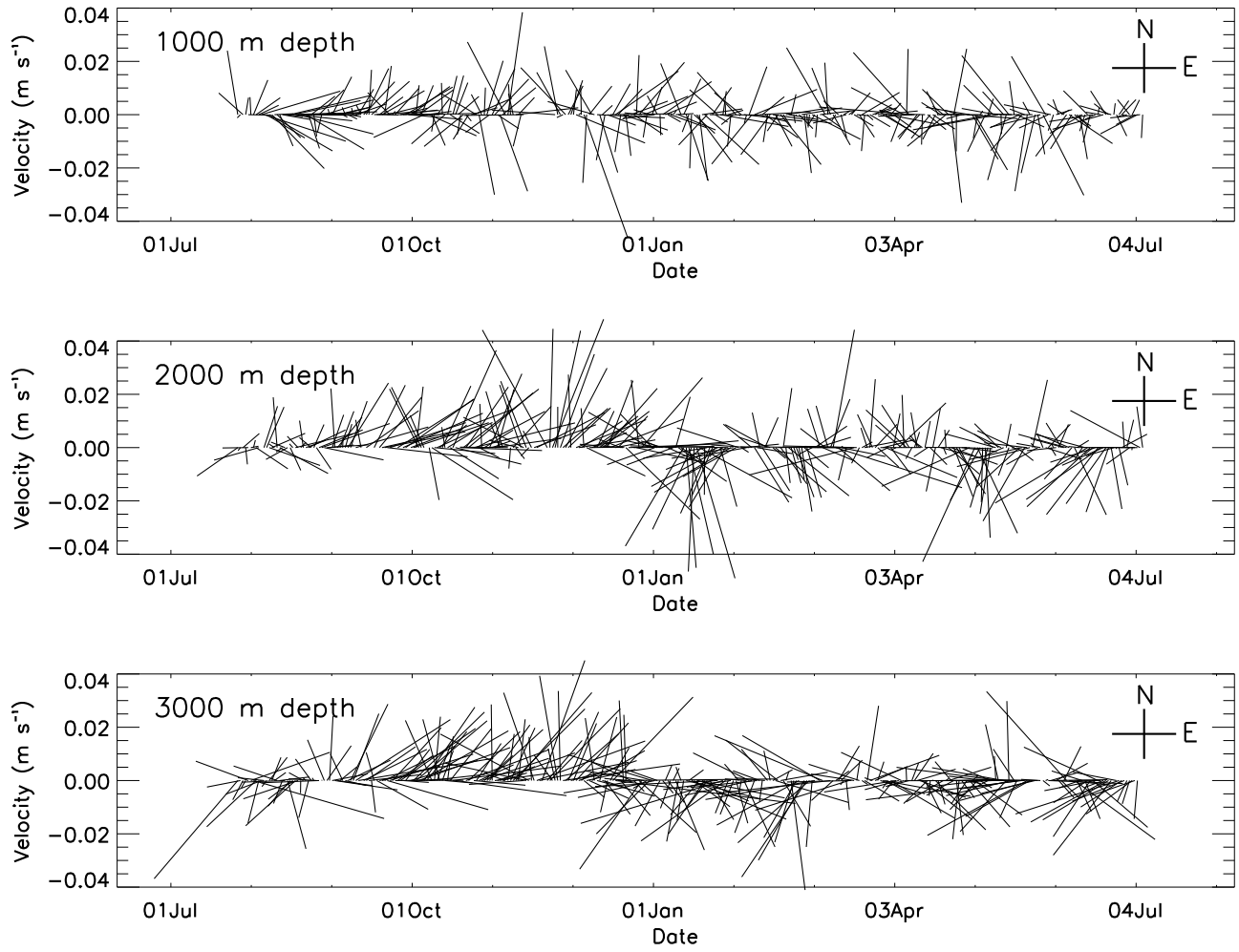

Figure 8. Time series of daily current velocities during our observation of current meters moored on the southern slope of the Suiko Seamount.

Figure 11 shows the climatological seasonally varying component (which is defined as anomaly from the annual mean component) of the Sverdrup transport estimated by integrating the wind stress curl over 171.6°E–229.7°E and averaging meridionally over 41.9°N–51.4°N. It is found that the seasonally varying component of the Sverdrup transport was northward (southward) from December to April (from May to November). If there is a boundary current along the eastern side of ESs, its direction should be opposite to that of the Sverdrup transport.

[26] The current meters moored on the southeastern slope of the Suiko Seamount were used again to investigate seasonal variations in the current along the eastern side of ESs. Figure 12 shows low-pass filtered daily current velocity anomalies relative to the annual mean obtained by taking the 40-day running mean to remove shorter fluctuations. Note that the amplitude ($\simeq$0.010 m s^{-1}) and direction (71.8° clockwise from the north) of the annual mean velocity at 1000 m depth (denoted by blue vector on the left side of each panel in Figure 12) almost corresponded to the amplitude (0.017 m s^{-1}) and direction (81.8° clockwise from the north) of the Argo float parking depth velocity at the cell of 44.0°N, 170.5°E on the mooring point (Figure 3). It is found that the seasonally varying component of the velocity changed from northward to southward in December at all three depths; the flow was southward (northward) from December to June (from August to November). The timing of this directional change corresponded well to the timing of the directional change in the interior Sverdrup transport from southward to northward (Figure 11). The period of the northward velocity component (August to November; Figure 12) was not inconsistent with that of the southward Sverdrup transport (Figure 11) although the opposite directional change from southward to northward in the daily moored velocity time series could not be confirmed owing to the lack of sampling from late June to early August (Figure 12). The weakening of the southward flow in March and April seemed to be due to eddies with periods less than 90 days. The coefficients of correlation between the meridional components of the daily moored velocities (Figure 12) and the interior Sverdrup transport obtained from the NCEP reanalysis data set in the same period were −0.60 at 1000 m depth, −0.54 at 2000 m depth and −0.70 at 3000 m depth. Therefore, the phase of the seasonally varying component of the velocities obtained from the current meters moored for 345 days (Figure 12) corresponded well to that of the climatological interior Sverdrup transport (Figure 11).

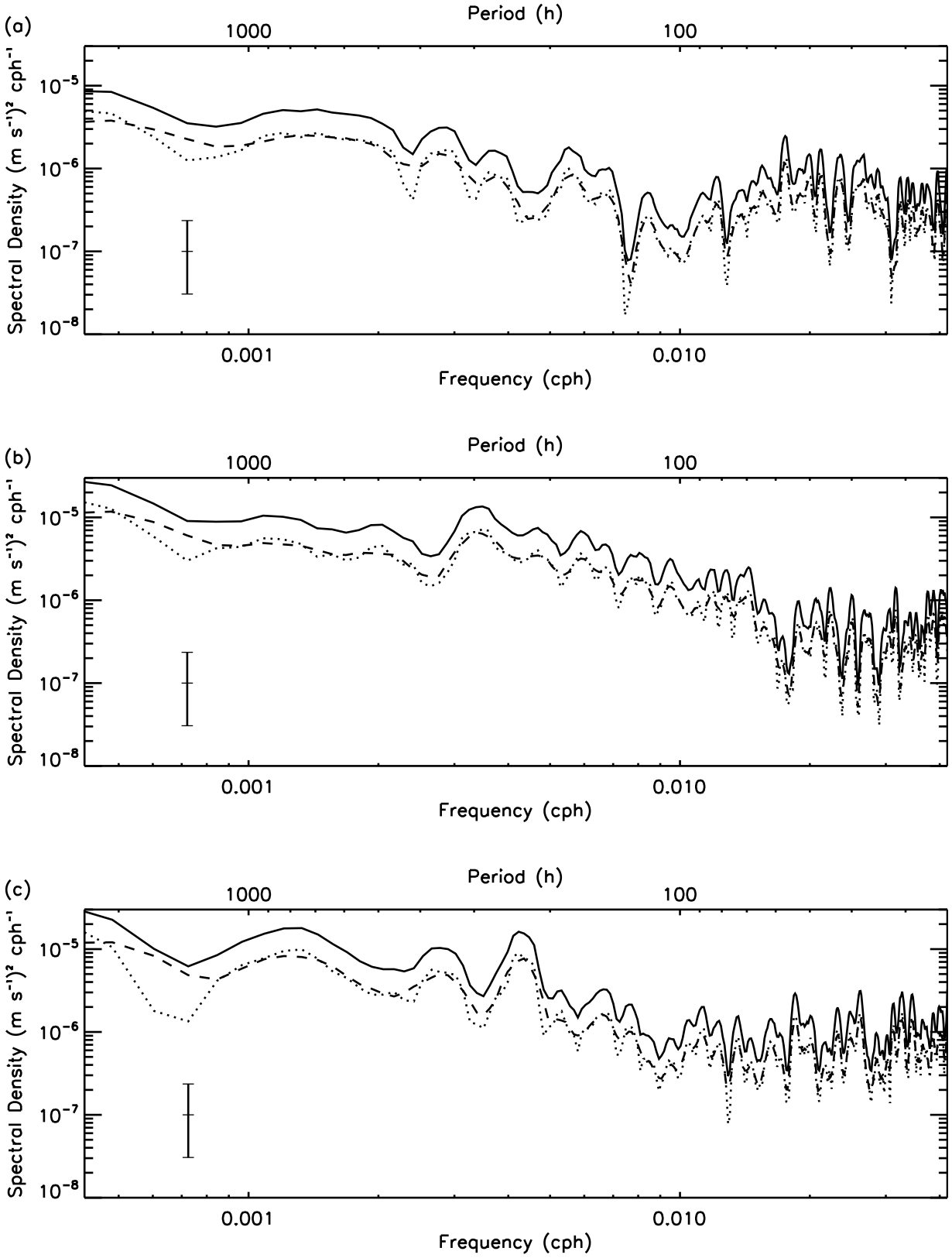

Figure 9. Rotary spectra ($m^2\ s^{-2}$ (cycle per hour)$^{-1}$) of the current velocity from current meters moored on the Suiko Seamount at (a) 1000 m, (b) 2000 m and (c) 3000 m depths. The total rotary spectra (solid thick lines) are shown in each diagram, as well as the clockwise (dotted lines) and anticlockwise (dashed lines) rotary components. Vertical bar is 95% confidence interval. The upper horizontal axis shows periods (unit: hour) whereas the lower horizontal axis represents frequency (unit: cycles per hour).

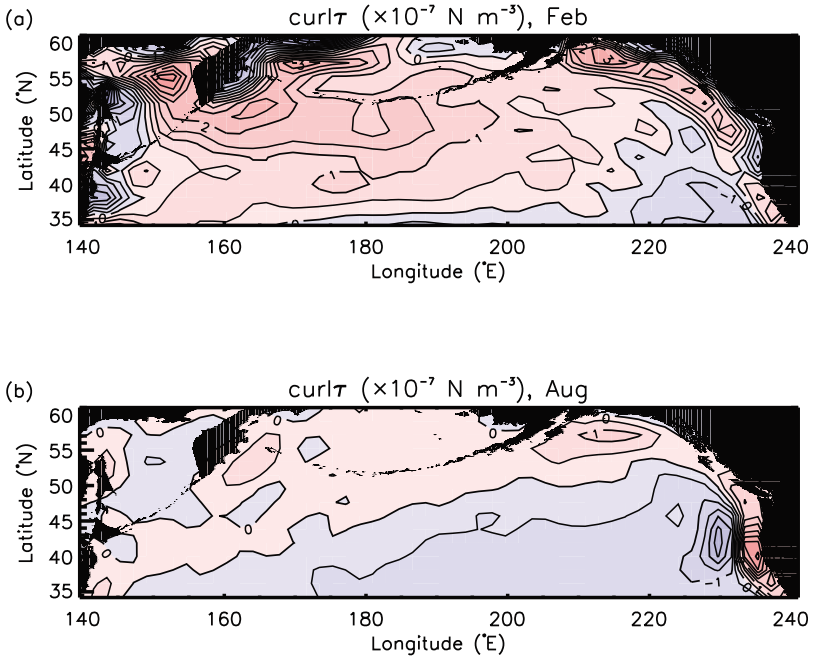

Figure 10. Horizontal distribution of the climatological monthly wind stress curl estimated from the NCEP reanalysis data set: (a) February and (b) August. Contour interval is 10^{-7} N m^{-3}.

[27] The vertical structure of the low-pass filtered velocities (Figure 12) was highly barotropic; root-mean square velocity fluctuations were about 0.010 m s^{-1}, 0.013 m s^{-1} and 0.012 m s^{-1} at 1000 m, 2000 m and 3000 m depth, respectively. These velocity amplitudes were of the same order (O (10^{-2} m s^{-1})) as those in *Kuragano and Kamachi* [2004] and *Wagawa et al.* [2010]. All the results strongly suggest the existence of boundary current along ESs, indicating that ESs divide the subarctic gyre of the North Pacific for shorter period fluctuations.

[28] To determine the horizontal structure of the boundary current, we attempted to extract the seasonal variation in the parking-depth velocities from the Argo float trajectories. We here adopted larger parameter and threshold (R_c = 2000 km and L_0 = 2500 km) and used the data in the extended region enclosed by red dotted lines in Figure 1 (35.0°N–55.0°N and 142.0°E–210.0°E) to extract the flow field of large-scale subarctic gyre of the North Pacific. Figures 13a and 13b show the velocity field at 1000 m depth in the 6-month mean (December to May (u_I) and June to November (u_{II})). The mean periods were determined on the basis of the magnitude of the climatological interior Sverdrup transport to the east of ESs (Figure 11). Although eastward flows dominate as suggested by *Reid* [1997] in both periods, there are also differences in these two velocity fields. In order to decompose the flow field into annual mean component and seasonally varying component, we also show $(u_I + u_{II})/2$ (which corresponds to the annual mean component) and $(u_I - u_{II})/2$ (which corresponds to the seasonally varying component) in Figures 13c and 13d, respectively. The annual mean field shows eastward flow as a whole, which corresponds to climatological flow field by *Reid* [1997]. Note that annual mean field is nontopographic because of the baroclinic Rossby wave adjustment. The seasonally varying component shows the southward current of a few cm s^{-1} along the eastern side of the ESs when the wind stress curl was positive (December to May; Figure 13d). Although the current was less clear in 45.5°N–47.5°N, we consider that it is caused by eddies which contaminate seasonally varying flow field. The seasonal change in current direction was consistent with that expected from the Sverdrup transport and its velocity amplitude was of the same order (O (10^{-2} m s^{-1})) as those in the moored current meters (Figure 12), *Kuragano and Kamachi* [2004] and *Wagawa et al.* [2010]. These results indicate that ESs divide

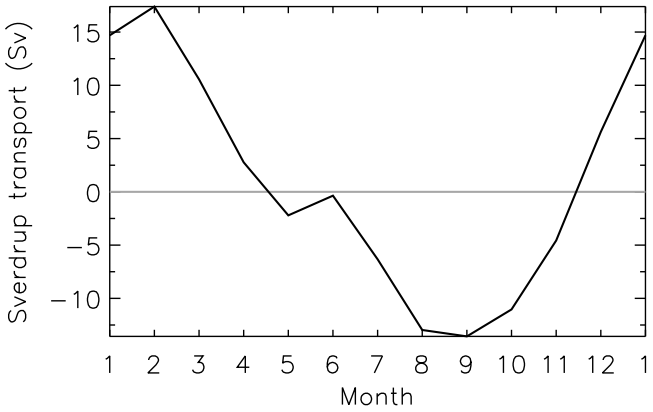

Figure 11. Seasonally varying component (anomaly from the annual mean component) of the interior Sverdrup transport to the east of the Emperor Seamounts (ESs) calculated from the climatological wind stress curl integrated from the eastern boundary to the ESs (171.6°E–229.7°E) and averaged meridionally over the region of 41.9°N–51.4°N.

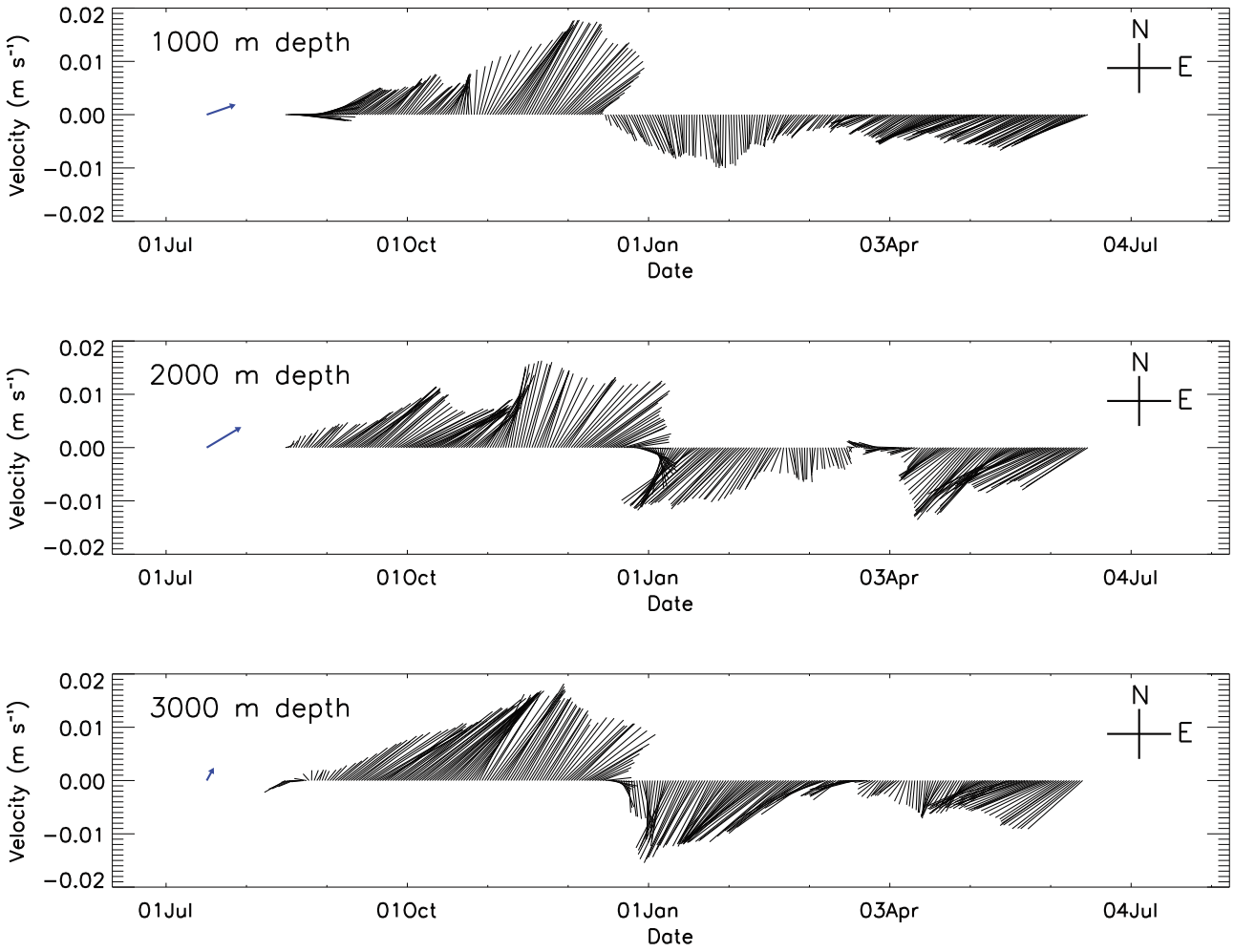

Figure 12. Same as Figure 8 except that shorter fluctuations are subtracted by taking the 40-day running mean and that the annual mean is removed. Blue vector on the left side of each panel indicates the annual component of the velocity at each depth.

the seasonally varying component of the subarctic gyre into two subgyres.

5. Summary and Discussion

[29] Bathymetric influences of Emperor Seamounts (ESs) on the flow fields in the subarctic North Pacific were investigated by analyzing data of the directly measured velocity. The influences were examined from two viewpoints: influences on the local flow field in the vicinity of ESs and influences on the large-scale subarctic gyre of the North Pacific. Climatological mean velocity fields were investigated for the former influences while seasonal variation in the current along the eastern side of ESs was examined for the latter influences. Our findings are:

[30] 1. Two relatively strong ($\sim$0.05 m s^{-1}) eastward flows were found at 1000 m depth. Notable deflections of these flows over ESs or the Shatsky Rise were identified. Eddies were also evident at 1000 m depth.

[31] 2. A Taylor cap that causes anticyclonic deflection induced by the eastward flow impinging against the Nintoku Seamount (42.0°N) was clearly identified in the climatological flow field. This feature was also identified in the near-surface flow field (15 m depth) and dynamic height field at 200 dbar relative to 2000 dbar. These results elucidate that the Taylor cap over the Nintoku seamount is stable or frequently generated and extends to the surface layer.

[32] 3. An anticyclonic flow was found over the Suiko Seamount (45.0°N). It was difficult to explain the generation of this flow using only the Taylor cap theory.

[33] 4. Data obtained from the current meter moored over the southeastern flank of the Suiko Seamount suggest that the boundary current partially compensates for the Sverdrup transport to the east of ESs. This boundary current was also detected in the Argo float trajectories.

[34] Although anticyclonic flows were found over both the Nintoku and Suiko Seamounts, their generation mechanisms seem different. The different mechanisms result in different distributions of water properties and nutrients; the Taylor cap induces continuous upwelling to the left of the impinging flow (looking downstream) [*Chapman and Haidvogel*, 1992], while eddy-induced flows are not accompanied by such organized vertical motions since they are not generated by the impinging flow. Thus, continuous upwelling to the near-surface layer, which can contribute to local biological activity, is expected over the northwestern flank of the

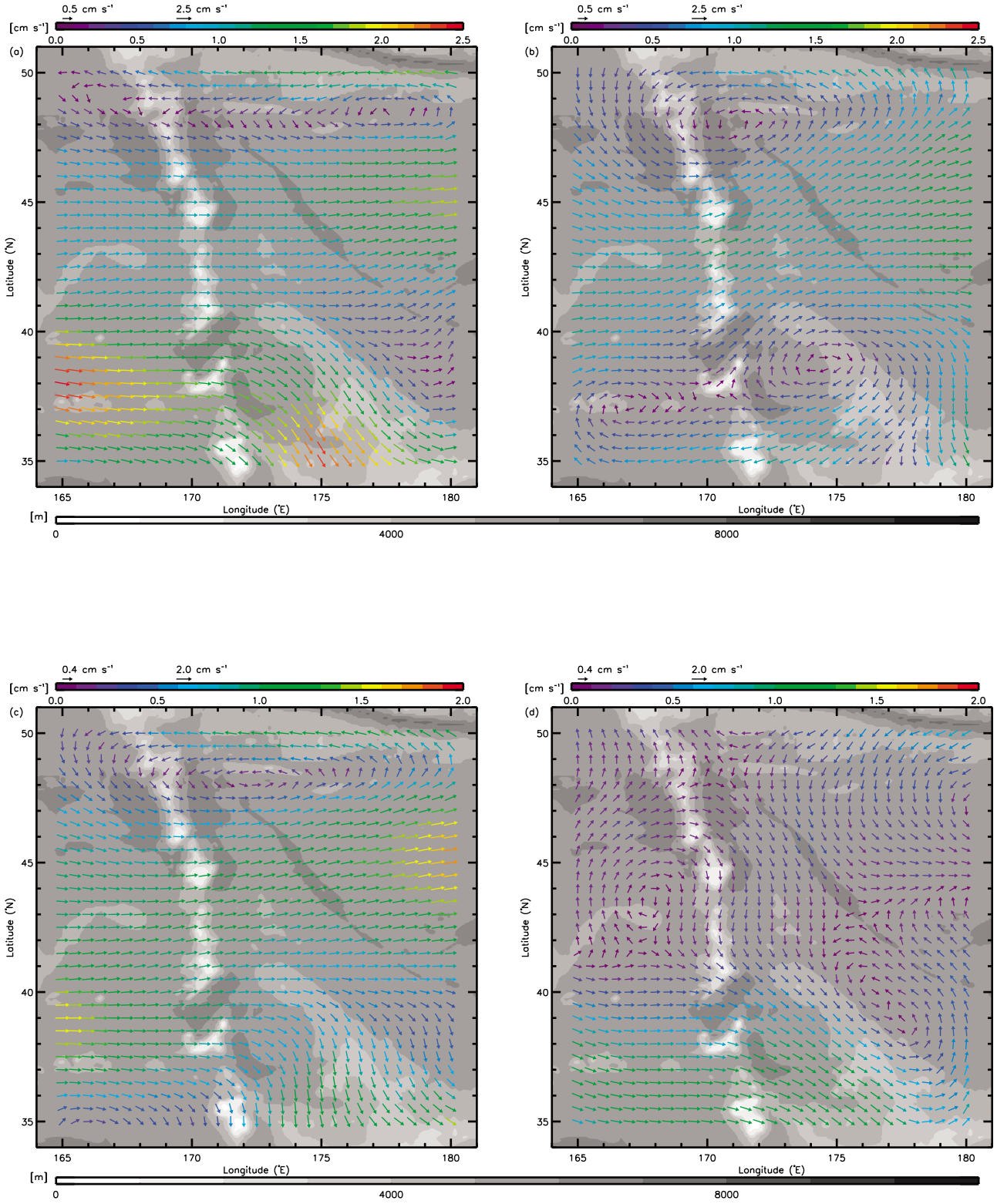

Figure 13. Velocity field of the 6-month mean ((a) December to May (u_I) and (b) June to November (u_{II})), (c) the annual mean component (($u_I + u_{II}$)/2) and (d) the seasonally varying component (($u_I - u_{II}$)/2) (the ratios of the velocity estimation errors to the estimated velocities are less than 0.1). Here, larger parameter and threshold (R_c = 2000 km and L_0 = 2500 km) and the data in the large region enclosed by red dotted lines in Figure 1 (35.0°N–55.0°N and 142.0°E–210.0°E) are used. Both color and length of the arrow represent the velocity magnitude.

Nintoku Seamount, while such continuous upwelling may be transient or weak in terms of the climatological mean around the Suiko Seamount.

[35] The boundary current along the eastern side of ESs, as a result of the bathymetric influences of ESs on the large-scale subarctic gyre of the North Pacific, was found for the first time from velocity observations. This result is contrary to some previous studies [*Isoguchi et al.*, 1997; *Isoguchi and Kawamura*, 2006] regarding the bathymetric influences of ESs on the subarctic gyre as negligible. Note that bathymetric influences on the subarctic gyre will be reduced on a longer timescale [e.g., *Wagawa et al.* 2010]. Bathymetric influences on the subarctic gyres in the North Pacific should, thus, be separately discussed in terms of the timescale of circulation variations.

[36] To directly support the generation mechanisms of the anticyclonic flows found over the Nintoku and Suiko Seamounts, extensive observations for velocity and density field with detailed levels of precision and resolution are required. Numerical experiments will also be useful to investigate such dynamics. The observation period of the moored current meters was less than one year (345 days) in the present study. In addition, there were few moorings. To obtain the horizontal structure of the boundary current along ESs, several velocity observations along the eastern side of ESs with a high level of precision are needed; these observations would need to be sufficiently precise to estimate the volume transport and examine the spatial patterns of the transport, and sufficiently long to analyze their seasonal variation through harmonic or spectral analyses. In addition, a greater number of Argo float data would help clarify the bathymetric influences of ESs. We will carry out such work in future studies.

[37] **Acknowledgments.** We are grateful to the crew of the 169-th and 180-th cruises of the T/S Oshoro-Maru of Hokkaido University. The Argo float data used in this study were collected and made freely available by the International Argo Project and the national programs that contribute to it (http://www.argo.ucsd.edu, http://wo.jcommops.org/cgi-bin/WebObjects/Argo). Comments made by the other reviewers and the Associate Editor have significantly improved this study. We wish to thank Akira Masuda of Kyushu University, Jong-Hwan Yoon of Kyushu University, Atsuhiko Isobe of Ehime University and Kaoru Ichikawa of Kyushu University for their instructive comments. Hiroji Onishi of Hokkaido University helps to accomplish our mooring observation. Daisuke Ambe of National Research Institute of Fisheries Science and Masatoshi Sato of Tohoku National Fisheries Research Institute provided technical advice relating to surface buoys and the optimal interpolation, respectively.

References

Adcock, S., and D. P. Marshall (2000), Interactions between geostrophic eddies and the mean circulation over large-scale bottom topography, *J. Phys. Oceanogr.*, *30*(12), 3232–3238.

Book, J. W., M. Wimbush, S. Imawaki, H. Ichikawa, H. Uchida, and H. Kinoshita (2002), Kuroshio temporal and spatial variations south of Japan determined from inverted echo sounder measurements, *J. Geophys. Res.*, *107*(C9), 3121, doi:10.1029/2001JC000795.

Boyer, T., S. Levitus, H. Garcia, R. A. Locarnini, C. Stephens, and J. Antonov (2005), Objective analyses of annual, seasonal, and monthly temperature and salinity for the world ocean on a 0.25° grid, *Int. J. Clim.*, *25*(7), 931–945.

Bretherton, F. P., R. E. Davis, and C. B. Fandry (1976), A technique for objective analysis and design of oceanographic experiments applied to MODE-73, *Deep Sea Res. Oceanogr. Abstr.*, *23*, 559–582.

Chapman, D., and D. Haidvogel (1992), Formation of Taylor caps over a tall, isolated seamount in a stratified ocean, *Geophys. Astrophys. Fluid Dyn.*, *64*, 31–65.

Chen, S., B. Qiu, and P. Hacker (2007), Profiling float measurements of the recirculation gyre south of the Kuroshio Extension in May to November 2004, *J. Geophys. Res.*, *112*, C05023, doi:10.1029/2006JC004005.

Dietz, R. S. (1954), Marine geology of northwestern Pacific: Description of Japanese bathymetric chart 6901, *Geol. Soc. Am. Bull.*, *65*, 1199–1224.

Hansen, D. W., and P.-M. Poulain (1996), Quality control and interpolations of WOCE–TOGA drifter data, *J. Atmos. Oceanic Technol.*, *13*(4), 900–909.

Holloway, G. (1987), Systematic forcing of large-scale geophysical flows by eddy-topography interaction, *J. Fluid Mech.*, *184*, 463–476.

Isoda, Y., and D. Fukai (2004), Water mass characteristics around the transitional domain in the northern North Pacific, *SOLA*, *79*, 65–75.

Isoguchi, O., and H. Kawamura (2006), Seasonal to interannual variations of the western boundary current of the subarctic North Pacific by a combination of the altimeter and tide gauge sea levels, *J. Geophys. Res.*, *111*, C04013, doi:10.1029/2005JC003080.

Isoguchi, O., H. Kawamura, and T. Kono (1997), A study on wind-driven circulation in the subarctic North Pacific using TOPEX/POSEIDON altimeter data, *J. Geophys. Res.*, *102*(C6), 12,457–12,468.

Ito, S., K. Uehara, T. Miyao, H. Miyake, I. Yasuda, T. Watanabe, and Y. Shimizu (2004), Characteristics of SSH anomaly based on TOPPEX/POSEIDON altimetry and *in situ* measured velocity and transport of Oyashio on OICE, *J. Oceanogr.*, *60*(2), 425–437.

Kalnay, E., et al. (1996), The NCEP/NCAR 40-year reanalysis project, *Bull. Am. Meteorol. Soc.*, *77*(3), 437–471.

Kasai, H., H. Saito, A. Yoshimori, and S. Taguchi (1997), Variability in timing and magnitude of spring bloom in the Oyashio region, the western subarctic Pacific off Hokkaido, Japan, *Fish. Oceanogr.*, *6*(2), 118–129.

Kono, T., and Y. Kawasaki (1997), Results of CTD and mooring observations southeast of Hokkaido: Part 1. Annual velocity and transport variations in the Oyashio, *Bull. Hokkaido Natl. Fish. Inst.*, *61*, 65–81.

Kuragano, T., and M. Kamachi (2004), Balance of volume transports between horizontal circulation and meridional overturn in the North Pacific subarctic region, *J. Oceanogr.*, *60*(2), 439–451.

Lavender, K. L., W. B. Owens, and R. E. Davis (2005), The mid-depth circulation of the subpolar North Atlantic Oceans as measured by subsurface floats, *Deep Sea Res., Part 1*, *52*(5), 767–785.

Levine, E. R., and W. B. White (1981), Large-scale synoptic thermal fronts in the mid-latitude North Pacific from 1976–1978, *J. Geophys. Res.*, *86*(C7), 6567–6579.

Levine, E. R., and W. B. White (1983), Bathymetric influences upon the character of North Pacific fronts, 1976–1980, *J. Geophys. Res.*, *88*(C14), 9617–9625.

Mann, M. E., and J. Park (1996), Joint spatiotemporal modes of surface temperature and sea level pressure variability in the Northern Hemisphere during the last century, *J. Clim.*, *9*(9), 2137–2162.

Menna, M., and P. M. Poulain (2010), Mediterranean intermediate circulation estimated from Argo data in 2003–2010, *Ocean Sci.*, *6*(1), 331–343, doi:10.5194/os-6-331-2010.

Mizuno, K. (1995), Basin-scale hydrographic analysis and optimal interpolation method (in Japanese with English abstract), *Oceanogr. Jpn.*, *4*(3), 187–208.

Niiler, P. P., N. A. Maximenko, G. G. Panteleev, T. Yamagata, and D. B. Olson (2003), Near-surface dynamical structure of the Kuroshio Extension, *J. Geophys. Res.*, *108*(C6), 3193, doi:10.1029/2002JC001461.

Papoulis, A. (1972), *Probability, Random Variables, and Stochastic Processes*, 583 pp., McGraw-Hill, New York.

Park, J. J., K. Kim, B. A. King, and S. C. Riser (2005), An advanced method to estimate deep currents from profiling floats, *J. Atmos. Oceanic Technol.*, *22*(8), 1294–1304, doi:10.1175/JTECH1748.1.

Qiu, B. (2002), Large-scale variability in the midlatitude subtropical and subpolar North Pacific Ocean: Observations and causes, *J. Phys. Oceanogr.*, *32*(1), 353–375.

Reid, J. L. (1997), On the total geostrophic circulation of the Pacific Ocean: Flow patterns, tracers, and transports, *Prog. Oceanogr.*, *39*(4), 263–352.

Roden, G. I. (1984), Mesoscale oceanic fronts of the North Pacific, *Ann. Geophys.*, *2*(4), 399–410.

Roden, G. I. (1987), Effect of seamounts and seamounts chains on ocean circulation and thermohaline structure, in *Seamount, Islands, and Atolls*, *Geophys. Monogr. Ser.*, vol. 43, edited by B. H. Keating et al., pp. 335–354, AGU, Washington, D. C.

Roden, G. I., and B. A. Taft (1985), Effect of the Emperor Seamounts on the mesoscale thermohaline structure during the summer of 1982, *J. Geophys. Res.*, *90*(C1), 839–855.

Saijo, Y., and S. Ichimura (1960), Primary production in the northwestern Pacific Ocean, *J. Oceanogr. Soc. Jpn.*, *16*(3), 139–145.

Sekine, Y. (1999), Anomalous southward intrusion of the Oyashio east of Japan: 2. Two-layer numerical model, *J. Geophys. Res.*, *104*(C2), 3049–3058.

Takahashi, M., and S. Ichimura (1972), Some aspects of primary production in the northwestern Pacific Ocean, in *Biological Oceanography of the Northern Pacific Ocean*, edited by A. Y. Takenouti et al., pp. 218–229, Idemitsu Shoten, Tokyo.

Taniguchi, A. (1999), Differences in the structure of the lower trophic levels of pelagic ecosystems in the eastern and western subarctic, *Prog. Oceanogr.*, *43*(2), 289–315.

Taniguchi, A., and T. Kawamura (1972), Primary production in the Oyashio region with special reference to the subsurface chlorophyll maximum layer and phytoplankton-zooplankton relationships, in *Biological Oceanography of the Northern Pacific Ocean*, edited by A. Y. Takenouti et al., pp. 231–243, Idemitsu Shoten, Tokyo.

Verron, J., and C. LeProvost (1985), A numerical study of quasi-geostrophic flow over isolated topography, *J. Fluid Mech.*, *154*, 231–252.

Wagawa, T., Y. Isoda, N. Saitoh, T. Azumaya, and K. Sakaoka (2006), Hydrographic structural change in the transition domain around the Emperor Seamounts (in Japanese with English abstract), *Oceanogr. Jpn.*, *15*(3), 267–281.

Wagawa, T., Y. Yoshikawa, and A. Masuda (2010), Bathymetric influences of the Emperor Seamounts upon the subarctic gyre of the North Pacific: Examining boundary current dynamics along the eastern side of the mountain ridge with an idealized numerical model, *J. Oceanogr.*, *66*(2), 259–271.

Wang, L., and C. J. Koblinsky (1994), Influence of mid-ocean ridges on Rossby waves, *J. Geophys. Res.*, *99*(C12), 25,143–25,153.

White, W. B., and D. R. Cayan (1998), Quasi-periodicity and global symmetries in interdecadal upper ocean temperature variability, *J. Geophys. Res.*, *103*(C10), 21,335–21,354.

Willis, J. K., and L.-L. Fu (2008), Combining altimeter and subsurface float data to estimate the time-averaged circulation in the upper ocean, *J. Geophys. Res.*, *113*, C12017, doi:10.1029/2007JC004690.